RSC Advances

PAPER

View Article Online
View Journal | View Issue

Cite this: *RSC Adv.*, 2014, **4**, 50312

Synthesis of $NiSe_2$/reduced graphene oxide crystalline materials and their efficient electrocatalytic activity in dye-sensitized solar cells

Xiao Zhang, Tian-zeng Jing, Sheng-qi Guo, Guan-dao Gao* and Lu Liu*

Received 2nd September 2014
Accepted 24th September 2014

DOI: 10.1039/c4ra09656h

www.rsc.org/advances

We synthesized two kinds of $NiSe_2$ crystalline material grown on graphene (microsphere $NiSe_2$/RGO and octahedron $NiSe_2$/RGO) through a facile hydrothermal route. Their catalytic activities as the counter electrodes (CEs) in dye-sensitized solar cells (DSSCs) were investigated through *I–V* curves and conversion efficiency tests. Attributed to the outstanding carrier transfer properties of graphene nanosheets, the $NiSe_2$/graphene materials exhibited an excellent electrochemical performance, and microsphere $NiSe_2$/RGO showed a better electrocatalytic performance as the CE for the reduction of triiodide than that of Pt. Furthermore, Tafel polarization and electrical impedance spectroscopy (EIS) were performed to evaluate the electrocatalytic activity of the as-prepared CEs.

1. Introduction

Dye-sensitized solar cells (DSSCs) have attracted extensive interest all over the world because of their facile fabrication process, cost-effectiveness and relatively high power conversion efficiency (PCE).[1–6] The electrodes of a typical DSSC are a TiO_2 nanocrystalline photoanode and a platinum (Pt) counter electrode. During the power conversion process, the counter electrode (CE) carries electrons from the external circuit to the redox electrolyte and promotes the regeneration of I^- from I_3^-, thus the CE is an essential part of a DSSC and plays an important role in obtaining a high PCE. Conventionally, owing to the high conductivity, outstanding electrocatalytic activity, and good chemical stability, depositing platinum (Pt) on conductive glass always results in a high PCE when working as the CE. However, the expensiveness and scarcity of Pt greatly hinder its extensive use as a CE in DSSCs.[7–9] Therefore, it is necessary to synthesize new, inexpensive and efficient materials to replace Pt.

As an important class of chalcogenide materials, nickel selenide semiconductors have exhibited impressive electronic and magnetic properties. It has been found that nickel selenides can be used for several applications in the field of materials science, and they have drawn extensive attention over the past few decades.[10–14] $NiSe_2$ is a member of the transition metal chalcogenides, and it is a Pauli paramagnetic metal with a resistivity of less than 10^{-3} Ω cm.[15,16] Such a high electrical conductivity is quite favorable for energy storage materials.[17] Furthermore, $NiSe_2$ exhibits an excellent catalytic activity and is also an environmentally benign, narrow bandgap semiconductor material. Furthermore, its sources (Ni and Se) are inexpensive and abundant on Earth.[18] Thus, $NiSe_2$ is an ideal alternative to replace Pt as the CE of DSSCs,[18] and more attention should be paid to researching the use of $NiSe_2$ in DSSCs.

Graphene not only possesses a high specific surface area and excellent mechanical flexibility but is also electrochemically active and electrically conductive to collect electron from outside current.[19–21] Interconnected graphene scaffolds can serve as the "tentacle" to capture the injected electrons and as the "speedway" to enhance the electron-transport rate by suppressing the electron recombination.[22] It is considered to be an ideal substrate for the growth of functional nanomaterials in electrochemical devices.[23–25] Recent research showed that metallic oxide and metal sulfide nanomaterials, such as MoO_2, TiO_2, CoS and Bi_2S_3, have already been decorated well with graphene, and exhibited enhanced electronic and electrocatalytic properties.[26–31] Li *et al.* have successfully prepared nanocomposites of NiS_2 nanoparticles with reduced graphene oxide (NiS_2/RGO), and the NiS_2/RGO nanocomposites exhibited much higher catalytic activity than NiS_2 alone due to the synergetic catalysis of NiS_2 and RGO.[32] However, to the best of our knowledge, there are limited reports about $NiSe_2$ used in DSSCs, and no relevant research on $NiSe_2$/graphene used in DSSCs as the counter electrode so far.

Herein, we report a facile two-step strategy to prepare two kinds of $NiSe_2$ crystalline material grown on reduced graphene oxide (microsphere $NiSe_2$/RGO and octahedron $NiSe_2$/RGO), and used them as the CEs of DSSCs. The formation process and photovoltaic properties of the $NiSe_2$/RGO materials have been investigated. Both $NiSe_2$/RGO crystalline materials exhibited a high electrical conductivity and catalytic activity. In addition, the microsphere $NiSe_2$/RGO crystalline material showed a higher PCE than Pt. As far as we know, it is the first time that

Tianjin Key Laboratory of Environmental Remediation and Pollution Control, Nankai University, Tianjin 300071, China. E-mail: gaoguandao@nankai.edu.cn; liul@nankai.edu.cn

hybrid materials of $NiSe_2$/RGO have been applied as a prominent Pt-free counter electrode in DSSCs.

2. Experimental section

2.1 Synthesis of the microsphere $NiSe_2$/RGO crystalline material

To begin with, graphene oxide (GO) nanosheets were synthesized by a modified Hummers method.[33] Then, the microsphere $NiSe_2$/RGO crystalline material was successfully grown on reduced graphene oxide nanosheets through a two-step hydrothermal treatment: 5 ml of GO water suspension (the concentration is 10 mg ml^{-1}) and 0.681 g $NiCl_2 \cdot 6H_2O$ were added to 15 ml *n*-dimethylformamide. After stirring for about 2 h, 15 ml anhydrous ethylenediamine and 0.316 g selenium powder were added and the mixture was stirred for about 1 minute. Subsequently, the mixed solution was transferred into a 50 ml Teflon-lined stainless steel autoclave. After heating at 150 °C for 15 h, 0.5 g ascorbic acid working as the reducing agent was added to the cooled mixture solution and heated at 150 °C for 5 h. After being washed with deionized water and ethanol, the obtained $NiSe_2$/RGO samples were dried in air.

2.2 Synthesis of the octahedron $NiSe_2$/RGO crystalline material

The synthetic procedure for the octahedron $NiSe_2$/RGO crystalline material was almost the same as that for the microsphere $NiSe_2$/RGO crystalline material. The only difference was that *n*-dimethylformamide was changed to diethylenetriamine.

2.3 Characterization

The crystallinity and composition of the as-prepared samples were characterized by X-ray diffraction (XRD, D/max-2500, Japan Science), the morphology was studied by field emission scanning electron microscopy (FESEM, Nanosem 430, FEI).

2.4 Electrochemical measurements

0.1 g $NiSe_2$/RGO powder and 0.025 g PEG20000 (used as the dispersant and binder) were added to ethanol. A $NiSe_2$/RGO slurry was made by continuously stirring the mixture. Then, a film was made by wiping the $NiSe_2$/RGO slurry on FTO conductive glass (LOF, TEC-15, 15 W per square) with a doctor-blade. After its stabilization on the conductive glass, the $NiSe_2$/RGO counter electrode was finally prepared by heating the glass at 450 °C for 2 h under the protection of argon.

A commercial TiO_2 sol (Solaronix, Ti-Nanoxide T/SP) was used to prepare the TiO_2 film on FTO, also through the doctor-blade method, and the film was soaked in an N719 dye solution (in ethanol) for 24 h to obtain dye-sensitized TiO_2 electrodes. DSSCs were assembled by injecting the electrolyte into the aperture between the dye-sensitized TiO_2 electrode and the counter electrode. The liquid electrolyte was composed of 0.05 M I_2, 0.1 M LiI, 0.6 M 1,2-dimethyl-3-propylimidazolium iodide (DMPII), and 0.5 M 4-*tert*-butyl pyridine with acetonitrile as the solvent. Surlyn 1702 was used as the spacer between the two electrodes. The two electrodes were clipped together and solid paraffin was used as the sealant to prevent the electrolyte solution from leaking. The effective cell area was 0.25 cm^2. Photocurrent–voltage curves were measured with a Zahner IM6 electrochemical workstation with a Trusttech CHF-XM-500W source under simulated sun illumination (Global AM 1.5, 100 mW cm^{-2}).

3. Results and discussion

3.1 XRD analysis of GO, RGO, and the two kinds of $NiSe_2$/RGO crystalline materials

Fig. 1 shows the XRD patterns of GO, RGO, and the two kinds of $NiSe_2$/RGO crystalline material. For GO, there is a typical characteristic diffraction peak at 10°.[34] After being reduced by the ascorbic acid, this peak entirely disappears and a broad peak at ~23° appears instead, indicating that –OH, C=O and –COOH groups have been removed from GO to a great extent (Fig. 1a).[35,36] The two XRD patterns of the $NiSe_2$ samples are consistent with the standard card JCPDS 65-1843, with eleven

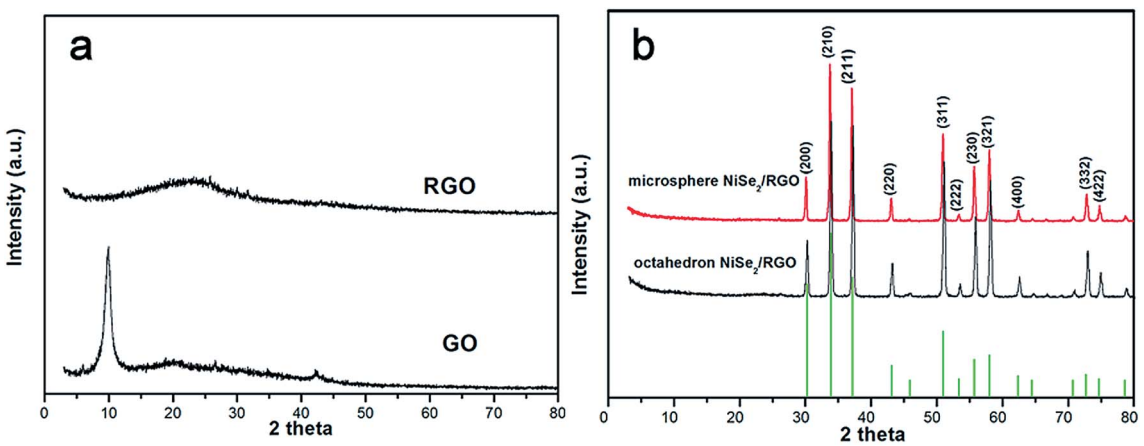

Fig. 1 XRD patterns of the GO, RGO (a) and $NiSe_2$/RGO crystalline materials (b).

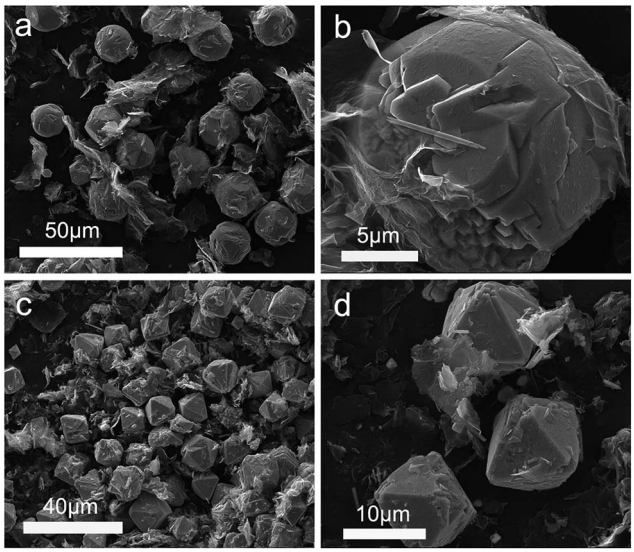

Fig. 2 SEM images of microsphere $NiSe_2$/RGO (a) and (b), and octahedron $NiSe_2$/RGO (c) and (d) at different magnifications.

obvious diffraction peaks at about 30.08°, 33.74°, 37.08°, 43.08°, 50.92°, 53.42°, 55.72°, 58.02°, 62.40°, 72.86° and 74.76°, corresponding to the (200), (210), (211), (220), (311), (222), (230), (321), (400), (332), (422) faces. Furthermore, there are no characteristic peaks for other impurities, showing that both samples are pure.

3.2 SEM analysis of the two kinds of $NiSe_2$/RGO crystalline materials

Fig. 2 displays the scanning electron microscopy (SEM) images of the as-synthesized samples with different magnifications. Graphene sheets spread with a little curl and wrap up the $NiSe_2$. Direct growth of the $NiSe_2$/graphene hybrids can be observed in the SEM images. Fig. 2a and c show the low-magnification SEM images of homogeneous $NiSe_2$ microspheres and octahedra respectively, with an average size of around 20 μm. The high magnification SEM images are shown in Fig. 2b and d. In Fig. 2b $NiSe_2$ microspheres consist of small particles, and $NiSe_2$ octahedra are composed of the microspheres.

3.3 Analysis of possible formation mechanisms

To investigate the formation process of both $NiSe_2$ crystalline materials, the relationship between the morphology of $NiSe_2$ and the synthesis time, as well as the presence of graphene, was investigated. We conducted time-dependent experiments with different synthesis times (1 h, 2 h, 4 h, 18 h + 1 h, 18 h + 2 h) and graphene-dependent (no RGO) experiments through comparing samples with and without graphene, and the SEM images are shown in Fig. 3 and 4, respectively.

For the microsphere $NiSe_2$/RGO, when the reaction time was very short (1 h), the morphology was tanglesome and particles with sizes of around tens of nanometers appeared (Fig. 3a). As the reaction time was increased (2 h, 4 h), particles gradually assembled together to form the sphere-like products and the morphology was not regular (Fig. 3b and c). After reaction for 18 h and reduction of graphene oxide for 1 h, the microspheres which were grown on graphene appeared (Fig. 3d). When the reduction time increased to 2 h, the microspheres were more regular (Fig. 3e). A similar formation process occurred for octahedron $NiSe_2$/RGO; at the initial stage of formation, irregular particles began to appear on the graphene sheets (Fig. 4a). When the reaction time was increased to 2 h and 4 h, the particles turned to rods and the rods assembled together to form an irregular bulk (Fig. 4b and c). After reaction for 18 h and reduction of graphene oxide for 1 h, an octahedron morphology began to appear, but it was not regular and there were holes (Fig. 4d). After further increasing the reduction time by one hour, regular octahedra could be clearly observed and the holes

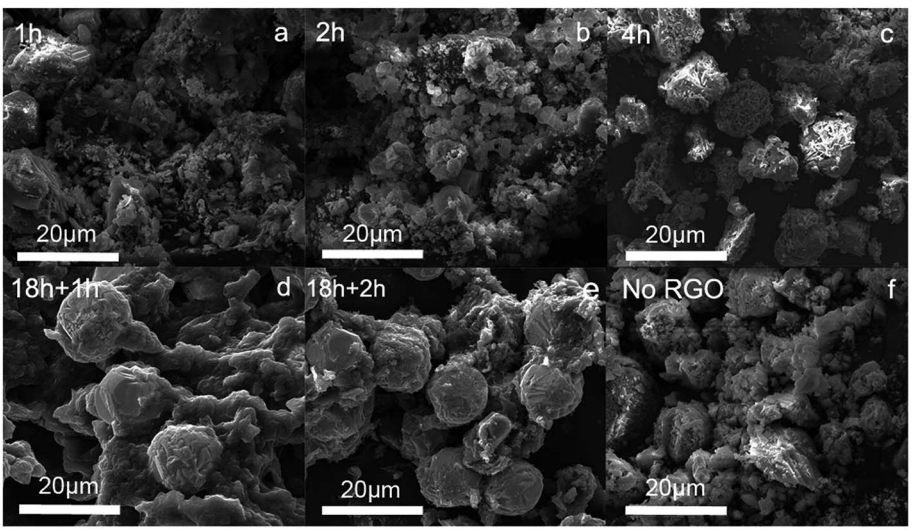

Fig. 3 SEM images of the microsphere $NiSe_2$/RGO samples prepared by different reaction times: (a) 1 h, (b) 2 h, (c) 4 h, (d) 18 h + 1 h, (e) 18 h + 2 h, and no RGO (f).

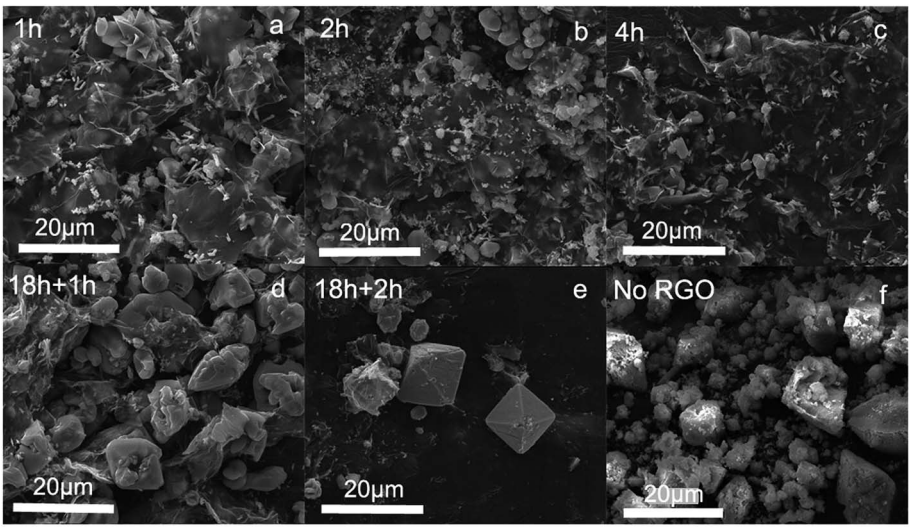

Fig. 4 SEM images of the octahedron $NiSe_2$/RGO samples prepared by different reaction times: (a) 1 h, (b) 2 h, (c) 4 h, (d) 18 h + 1 h, (e) 18 h + 2 h, and no RGO (f).

disappeared (Fig. 4e). Further studies on the influence of graphene on the formation process showed that addition of graphene was important for the formation of microspheres and octahedra (Fig. 3f and 4f). By comparing the SEM images, when there was no graphene, microspheres and octahedra could not be obtained and the morphology was tanglesome. These investigations revealed that the synthetic time and graphene addition are key parameters in the formation of microspheres and octahedra.

3.4 DSSCs performance analysis

The photovoltaic performances of DSSCs with CEs assembled by microsphere $NiSe_2$/RGO, octahedron $NiSe_2$/RGO, Pt and RGO under the illumination of 1 sun (100 mW cm^{-2}) are shown in Fig. 5, and the resultant photovoltaic parameters are listed in Table 1. When microsphere $NiSe_2$/RGO was used as the counter electrode, the resultant photovoltaic parameters were $V_{oc} = 0.73$ V, $J_{sc} = 15.82$ mA cm^{-2}, FF = 0.61, and $\eta = 6.94\%$. Accordingly, for the octahedron $NiSe_2$/RGO, these parameters were $V_{oc} = 0.71$ V, $J_{sc} = 15.96$ mA cm^{-2}, FF = 0.55 and $\eta = 6.23\%$. Compared with the above two $NiSe_2$ crystalline materials, the photovoltaic performance of RGO was poorer (for RGO, $V_{oc} = 0.77$ V, $J_{sc} = 12.81$ mA cm^{-2}, FF = 0.41, $\eta = 4.05\%$). The microsphere $NiSe_2$/RGO CE possessed the best catalytic activity, which was slightly inferior to the Pt-based CE ($\eta = 6.82\%$). Based on the test data, microsphere $NiSe_2$/RGO showed a higher FF than the other CEs, which reveals a more efficient use of photogenerated electrons. For the reason that the graphene film provided a large surface area for the reduction of I_3^- and its ability to receive electrons, the transfer speed of the electrons was accelerated. Thus, it is advantageous for the electron transfer from the electrode to the I_3^-. Furthermore, $NiSe_2$/RGO possessed a high catalytic activity for the reduction of I_3^-, and eventually resulted in a high PCE for $NiSe_2$/RGO crystalline materials.

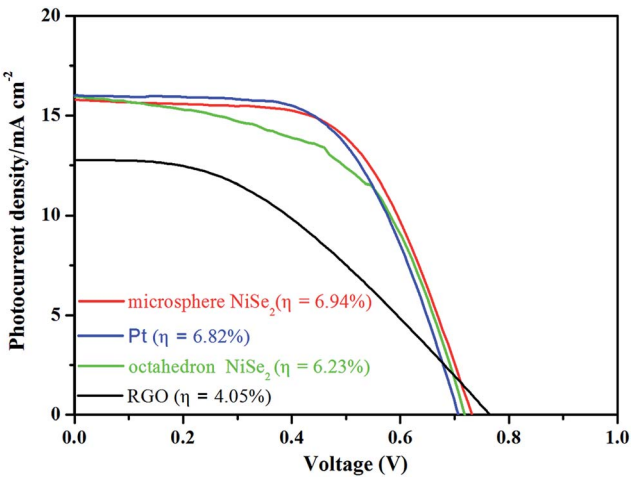

Fig. 5 Photocurrent density–voltage characteristics of DSSCs with different CEs.

3.5 Tafel polarization curves analysis

Fig. 6 shows the Tafel polarization curves of the different CEs which were measured using the dummy cells. Generally, the Tafel polarization curve can be divided into three zones: polarization zone (low potential, $|V| < 120$ mV), Tafel zone (intermediate potential with a sharp slope), and diffusion zone (high potential). In the Tafel zone, strictly speaking, the curve should be a straight line, and exchange current density (J_0) can be obtained by intersecting the cathodic branch of the Tafel zone and the equilibrium potential line.[37] In the diffusion zone, the curve is almost a horizontal line, indicating that as the potential increases the current intensity does not change any more. Furthermore, the diffusion current density at this time is the limiting diffusion current density (J_{lim}). The higher J_0 and J_{lim} indicate a better catalytic activity for reducing I_3^- and a bigger diffusion coefficient of I_3^-, respectively.[38] Both J_0 and J_{lim}

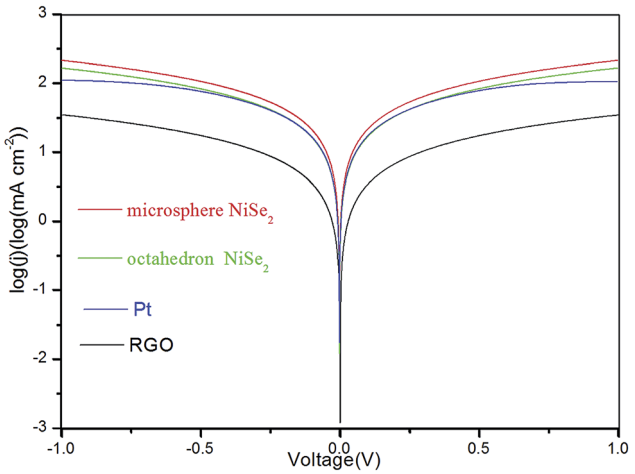

Fig. 6 Tafel polarization curves of symmetrical cells fabricated with different CEs that are the same as the ones used in the EIS experiments.

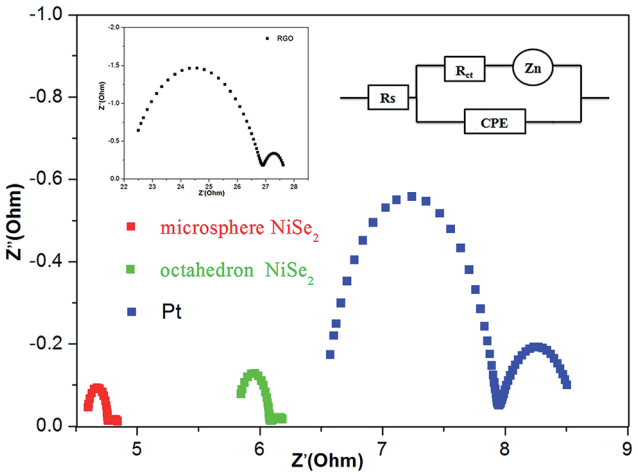

Fig. 7 Nyquist plots for symmetric cells fabricated with different CEs, the inset gives the Nyquist plots of RGO and the equivalent circuit.

increase in the order of RGO < octahedron $NiSe_2$/RGO < microsphere $NiSe_2$/RGO, which is fairly consistent with the PCE and electrical impedance spectroscopy analysis. This tendency also proved that microsphere $NiSe_2$/RGO owned the best catalytic activity among the CEs. The variation of J_0 is closely associated with the charge transfer resistance (R_{ct}) according to eqn (1)

$$J_0 = \frac{RT}{nFR_{ct}} \quad (1)$$

where R is the gas constant, T is the temperature, F is Faraday's constant, n is the total number of electrons involved in the reaction, and R_{ct} is the charge transfer resistance.

3.6 EIS measurements analysis

For further evaluating the electrocatalytic activity of the as-prepared CEs for the reduction of triiodide, electrical impedance spectroscopy (EIS) tests were carried out using symmetric cells fabricated with two identical CEs (CE/electrolyte/CE). For comparison, EIS tests of microsphere $NiSe_2$/RGO, octahedron $NiSe_2$/RGO, Pt and RGO were performed. As shown in Fig. 7, the Nyquist plots for symmetric cells with different CEs illustrate impedance characteristics, in which two semicircles are observed. The high-frequency intercept on the real axis (Z'-axis) represents the series resistance (R_s), and the semicircle in the high-frequency region (left) stems from the charge-transfer resistance (R_{ct}) and the constant phase element (CPE) at the CE/electrolyte interface. Another semicircle in the low frequency range (right) arises from resistance at the $NiSe_2$/electrolyte interface and the triiodide/iodide redox couple Nernst diffusion impedance (Z_N) in the electrolyte.[32] R_s accounts for the resistance within the bulk of the electrolyte, the electrodes, the contact resistance at joints, *etc.* The ions in the electrolyte accumulate at the electrode/electrolyte interface and produce a capacitance there, which can be modeled by the CPE. The R_{ct} values of microsphere $NiSe_2$/RGO and octahedron $NiSe_2$/RGO were found to be 0.15 Ω and 0.25 Ω, respectively, which were lower than the value of 1.43 Ω for a Pt electrode. The smallest R_{ct} reveals the highest catalytic ability of microsphere $NiSe_2$/RGO.[39] The catalytic ability of CE materials was significantly influenced by the effective active site at which the $NiSe_2$/RGO films might be larger than the Pt film.[40] Furthermore, microsphere $NiSe_2$/RGO CE owned the smallest R_s among all of the CEs, which was beneficial for FF.[41] More resistance and impedance values are listed in Table 1.

4. Conclusion

In summary, two kinds of $NiSe_2$ crystalline material have been successfully synthesized and grown on reduced graphene oxide using a facile hydrothermal reaction. We have demonstrated that high electrical conductivity and catalytic activity can be simultaneously achieved by using the $NiSe_2$/RGO materials as the CEs of DSSCs, which exhibited highly catalytic properties

Table 1 Photovoltaic and electrochemical performance parameters for different CE

CE	V_{oc} (V)	J_{SC} (mA cm^{-2})	FF	η (%)	R_S (Ω cm^2)	R_{ct} (Ω cm^2)
Microsphere $NiSe_2$/RGO	0.73	15.82	0.61	6.94	4.58	0.15
Octahedron $NiSe_2$/RGO	0.71	15.96	0.55	6.23	5.81	0.25
Pt	0.71	16.00	0.60	6.82	6.49	1.43
RGO	0.77	12.81	0.41	4.05	22.03	4.89

with respect to I^-/I_3^- redox reactions and could be potentially used as CE materials in DSSCs. This study advances the development of $NiSe_2$ applied in the CE of DSSCs and stimulates us to devote more time to the research for improving the photoelectric properties of $NiSe_2$.

Acknowledgements

This work was supported by the National Science Foundation of China (No. 21271108), 2011 Science Foundation of Tianjin (No. 11JCZDJC24800), and China–U.S. Center for Environmental Remediation and Sustainable Development.

References

1 B. O'Regan and M. Grätzel, *Nature*, 1991, **353**, 737–740.
2 A. Yella, H. W. Lee, H. N. Tsao, C. Y. Yi, A. K. Chandiran, M. K. Nazeeruddin, E. W. G. Diau, C. Y. Yeh, S. M. Zakeeruddin and M. Grätzel, *Science*, 2011, **334**, 629–634.
3 M. J. Ju, J. Kim, C. H. J. Choi, I. T. Choi, S. G. Kim, K. Lim, J. Ko, J. J. Lee, I. Y. Jeon, J. B. Baek and H. K. Kim, *ACS Nano*, 2013, **7**, 5243–5250.
4 A. Hagfeldt, G. Boschloo, L. C. Sun, L. Kloo and H. Pettersso, *Chem. Rev.*, 2010, **110**, 6595–6663.
5 M. X. Wu, X. Lin, Y. D. Wang, L. Wang, W. Guo, D. D. Qi, X. J. Peng, A. Hagfeldt, M. Grätzel and T. L. Ma, *J. Am. Chem. Soc.*, 2012, **134**, 3419–3428.
6 J. M. Lim, H. A. Kim, B. H. Kim, C. H. Han and Y. S. Jun, *RSC Adv.*, 2014, **4**, 243–247.
7 H. J. Chen, Y. A. Xie, H. L. Cui, W. Zhao, X. L. Zhu, Y. M. Wang, X. J. Lu and F. Q. Huang, *Chem. Commun.*, 2014, **50**, 4475–4477.
8 H. C. Sun, D. Qin, S. Q. Huang, X. Z. Guo, D. M. Li, Y. H. Luo and Q. B. Meng, *Energy Environ. Sci.*, 2011, **4**, 2630–2637.
9 P. W. Chen, C. P. Lee, L. Y. Chang, J. Chang, M. H. Yeh, L. Y. Lin, R. Vittal, J. J. Lin and K. C. Ho, *RSC Adv.*, 2013, **3**, 5871–5881.
10 C. E. M. Campos, J. C. de Lima, T. A. Grandi, K. D. Machado, J. P. Itie and A. Polian, *J. Solid State Chem.*, 2005, **178**, 93–99.
11 M. A. Petrukhina, C. Henck, B. Li, E. Block, J. Jin, S. Z. Zhang and R. Clerac, *Inorg. Chem.*, 2005, **44**, 77–84.
12 X. G. Peng, L. Manna, W. D. Yang, J. Wickham, E. Scher, A. Kadavanich and A. P. Alivisatos, *Nature*, 2000, **404**, 59–61.
13 X. Yu, W. D. Sun and Y. Chu, *New J. Chem.*, 2014, **38**, 70–76.
14 M. R. Gao, Z. Y. Lin, T. T. Zhuang, J. Jiang, Y. F. Xu, Y. R. Zheng and S. H. Yu, *J. Mater. Chem.*, 2012, **22**, 13662–13668.
15 S. Ogawa, *J. Appl. Phys.*, 1979, **50**, 2308–2311.
16 J. M. Honig and J. Spalek, *Chem. Mater.*, 1998, **10**, 2910–2929.
17 M. Z. Xue and Z. W. Fu, *Electrochem. Commun.*, 2006, **8**, 1855–1862.
18 F. Gong, X. Xu, Z. Q. Li, G. Zhou and Z. S. Wang, *Chem. Commun.*, 2013, **49**, 1437–1439.
19 Z. P. Chen, W. C. Ren, L. B. Gao, B. L. Liu, S. F. Pei and H. M. Cheng, *Nat. Mater.*, 2011, **10**, 424–428.
20 X. Huang, Z. Y. Yin, S. Wu, X. Y. Qi, Q. Y. He, Q. C. Zhang, Q. Y. Yan, F. Boey and H. Zhang, *Small*, 2011, **7**, 1876–1902.
21 Z. Y. Yin, J. X. Zhu, Q. Y. He, X. H. Cao, C. L. Tan, H. Y. Chen, Q. Y. Yan and H. Zhang, *Adv. Energy Mater.*, 2014, **4**, 1300574–1300592.
22 F. Xu, J. Chen, X. Wu, Y. Zhang, Y. X. Wang, J. Sun, H. C. Bi, W. Lei, Y. R. Ni and L. T. Sun, *J. Phys. Chem. C*, 2013, **117**, 8619–8627.
23 S. J. Park and R. S. Ruoff, *Nat. Nanotechnol.*, 2009, **4**, 217–224.
24 H. L. Wang, J. T. Robinson, G. Diankov and H. J. Dai, *J. Am. Chem. Soc.*, 2010, **132**, 3270–3271.
25 H. L. Wang, Y. Yang, Y. Y. Liang, L. F. Cui, H. S. Casalongue, Y. G. Li, G. S. Hong, Y. Cui and H. J. Dai, *Angew. Chem., Int. Ed.*, 2011, **50**, 7364–7368.
26 Y. M. Sun, X. L. Hu, W. Luo and Y. H. Huang, *ACS Nano*, 2011, **5**, 7100–7107.
27 S. B. Yang, X. L. Feng and K. Müllen, *Adv. Mater.*, 2011, **23**, 3575–3579.
28 C. Chen, W. M. Cai, M. C. Long, B. X. Zhou, Y. H. Wu, D. Y. Wu and Y. J. Feng, *ACS Nano*, 2010, **4**, 6425–6432.
29 X. H. Miao, K. Pan, G. F. Wang, Y. P. Liao, L. Wang, W. Zhou, B. J. Jiang, Q. J. Pan and G. H. Tian, *Chem.–Eur. J.*, 2014, **20**, 474–482.
30 Y. Gu, Y. Xu and Y. Wang, *ACS Appl. Mater. Interfaces*, 2013, **5**, 801–806.
31 G. Li, X. S. Chen and G. D. Gao, *Nanoscale*, 2014, **6**, 3283–3288.
32 C. Y. Su, Y. P. Xu, W. J. Zhang, J. W. Zhao, X. H. Tang, C. H. Tsai and L. J. Li, *Chem. Mater.*, 2009, **21**, 5674–5680.
33 Z. Q. Li, F. Gong, G. Zhou and Z. S. Wang, *J. Phys. Chem. C*, 2013, **117**, 6561–6566.
34 C. Nethravathi and R. Michael, *Carbon*, 2008, **46**, 1994–1998.
35 D. P. He, K. Cheng, T. Peng, X. L. Sun, M. Pan and S. C. Mu, *J. Mater. Chem.*, 2012, **22**, 21298–21304.
36 J. F. Shen, B. Yan, M. Shi, H. W. Ma, N. Li and M. X. Ye, *J. Mater. Chem.*, 2011, **21**, 3415–3421.
37 Q. Zhang, Y. F. Liu, Y. D. Duan, N. Q. Fu, Q. P. Liu, Y. Y. Fang, Q. W. Sun and Y. Lin, *RSC Adv.*, 2014, **4**, 15091–15097.
38 J. H. Guo, Y. T. Shi, C. Zhu, L. Wang, N. Wang and T. L. Ma, *J. Mater. Chem. A*, 2013, **1**, 11874–11879.
39 J. Y. Park, J. H. Noh, T. N. Mandal, S. H. Im, Y. Jun and S. Seok, *RSC Adv.*, 2013, **3**, 24918–24921.
40 S. H. Chang, M. D. Lu, Y. L. Tung and H. Y. Tuan, *ACS Nano*, 2013, **7**(10), 9443–9451.
41 H. J. Chen, Y. Xie, H. L. Cui, W. Zhao, X. L. Zhu, Y. M. Wang, X. J. Lu and F. Q. Huang, *Chem. Commun.*, 2014, **50**, 4475–4477.